J. Fluid Mech. (2001), *vol.* 426, *pp.* 387–396. Printed in the United Kingdom

Fluid flows in precessing spherical shells

By A. TILGNER AND F. H. BUSSE

Institute of Physics, University of Bayreuth, D-95440 Bayreuth, Germany

(Received 9 July 2000 and in revised form 27 September 2000)

Numerical solutions for fluid flows in precessing spherical cavities and spherical shells have been obtained and are compared with earlier analytical expressions. It is shown that the approximate validity of the analytical expressions extends further than could have been expected. The details of the flow structure exhibit significant departures, however, from the assumptions of the analytical theory. Standing waves are found in the case of sufficiently thin shells. Some results on instabilities of the basic flow are also discussed.

1. Introduction

The flow of an incompressible fluid contained in a precessing spherical cavity is one of the basic problems of fluid dynamics. Traditionally it has been considered as a special limit of the more general problem of fluid flows in precessing spheroidal cavities. The interest in the latter type of flow arose in the 19th century when the effects of the precession of celestial bodies on their fluid interiors were discussed. At that time the viscosity of the fluid was neglected and only the coupling between fluid and container due to pressure forces was considered. For a review of this work we refer to Lamb's (1932) treatise. In general, both viscous stresses exerted by the containing rigid surfaces and pressure gradients contribute to the coupling, and the special case of precessing spherical fluid shells is distinguished by the property that the effect of the pressure vanishes. Analytical studies have usually been restricted to cases without inner boundaries. The linear problem of flows in precessing spheroidal cavities has been considered by Stewartson & Roberts (1963) and Roberts & Stewartson (1965). The results of this theory are valid as long as the angle ε between the axis of the average rotation of the fluid and the axis of the container is sufficiently small. The linear analysis was extended by Busse (1968) into the nonlinear regime in that terms of the order ε^2 were taken into account.

Numerical calculations have been hampered until recently by the high computational costs of resolving the thin Ekman layers close to the rigid boundaries. Within the past few years Ekman numbers of the order 10^{-4} have become computationally accessible. Hollerbach & Kerswell (1995) have studied the spin-over mode which is closely related to precession-driven flow at low precession rates. These authors focused on the structure of internal shear layers. Stationary flow in precessing spherical shells has been simulated by Tilgner (1999*b*) who found deviations from a solid body rotation on large spatial scales as well as the localized shear layers. Here, we study these deviations in considerably more detail and compare quantitatively analytical and numerical results. We also consider shells with a large inner core in which case inertial oscillations are excited. Besides the flows which are stationary in the precessing frame of reference, unsteady flows evolving from an instability of the steady flow have also been found as will be demonstrated in § 6 of this paper.

2. Mathematical formulation of the problem and numerical methods

We consider a fluid-filled spherical shell of thickness d which is rotating with angular velocity ω. Using d and $1/\omega$ as units of length and time, we can write the non-dimensional equations for the velocity field in a frame of reference attached to the precessing spherical shell (hereafter called the 'mantle system') in the form

$$\frac{\partial}{\partial t}\boldsymbol{u} + (\nabla \times \boldsymbol{u}) \times \boldsymbol{u} + 2(\hat{\boldsymbol{z}} + \boldsymbol{\Omega}) \times \boldsymbol{u} = -\nabla\pi + E\nabla^2\boldsymbol{u} - (\boldsymbol{\Omega} \times \hat{\boldsymbol{z}}) \times \boldsymbol{r}, \tag{2.1a}$$

$$\nabla \cdot \boldsymbol{u} = 0. \tag{2.1b}$$

Hats denote unit vectors. The Ekman number E is defined by $E = \nu/d^2\omega$ where ν is the kinematic viscosity. π stands for a reduced pressure which can be dropped from the analysis because only the curl of (2.1a) will be used. The z-axis of a Cartesian system of coordinates (x, y, z) is fixed to the mantle in the direction of its axis of rotation. $\boldsymbol{\Omega}$ is the precession vector and its direction forms an angle $\alpha(0 < \alpha \leqslant \frac{1}{2}\pi)$ with the z-axis. Its time dependence in the mantle system is given by

$$\boldsymbol{\Omega} = \Omega(\hat{\boldsymbol{x}} \sin\alpha \cos t - \hat{\boldsymbol{y}} \sin\alpha \sin t + \hat{\boldsymbol{z}} \cos\alpha). \tag{2.2}$$

Retrograde precession corresponds to $\Omega < 0$. The boundary conditions require

$$\boldsymbol{u} = 0 \quad \text{at} \quad r = r_i = \eta(1-\eta)^{-1} \quad \text{and at} \quad r = r_o = (1-\eta)^{-1} \tag{2.3}$$

where η is the ratio of the radii of the shell. The solenoidal field $\boldsymbol{u}$ can be written in terms of the poloidal and toroidal scalars v and w,

$$\boldsymbol{u} = \nabla \times \nabla \times (v\hat{\boldsymbol{r}}) + \nabla \times (w\hat{\boldsymbol{r}}). \tag{2.4}$$

The functions v and w can be decomposed into radial and angular parts

$$v = r\sum_{l=1}^{\infty}\sum_{m=-l}^{l} V_l^m(r,t)P_l^m(\cos\theta)\mathrm{e}^{\mathrm{i}m\varphi}, \quad w = r^2\sum_{l=1}^{\infty}\sum_{m=-l}^{l} W_l^m(r,t)P_l^m(\cos\theta)\mathrm{e}^{\mathrm{i}m\varphi} \tag{2.5}$$

where a spherical system of coordinates (r, θ, φ) has been introduced and where $P_l^m(\cos\theta)$ denotes the associated Legendre functions. Operating with $\hat{\boldsymbol{r}} \cdot \nabla\times$ and $\hat{\boldsymbol{r}} \cdot \nabla \times \nabla\times$ on (2.1a) and projecting the result onto the system of spherical harmonics one obtains two sets of equations for the functions $V_l^m(r,t)$ and $W_l^m(r,t)$. These equations have to be solved subject to the boundary conditions

$$V_l^m = \frac{\partial V_l^m}{\partial r} = W_l^m = 0 \quad \text{at} \quad r = r_i \equiv \eta/(1-\eta) \quad \text{and at} \quad r = r_o \equiv (1-\eta)^{-1}. \tag{2.6a}$$

If the inner boundary is stress-free, the condition at $r = r_i$ is replaced by

$$V_l^m = \frac{\partial^2 V_l^m}{\partial r^2} = \frac{\partial W_l^m}{\partial r} = 0. \tag{2.6b}$$

For the numerical solution of the equations for $V_l^m(r,t)$, $W_l^m(r,t)$ a pseudo-spectral method is used and a Chebychev collocation scheme is employed in the radial direction. All nonlinear products are computed in direct space. The time stepping scheme differs slightly from the version that has been used in earlier work on convection in spherical shells (Tilgner 1996; Tilgner & Busse 1997). The nonlinear terms, the diffusion terms and the forcing f are treated with second-order Adams–Bashforth, implicit-Euler and Crank–Nicholson steps, respectively. The rationale behind this time stepping scheme and issues of resolution are discussed in a separate publication

(Tilgner 1999*a*). The direct simulations described in the next section have required resolutions of up to 65 Chebychev polynomials and spherical harmonics of degree up to 64. Occasional runs have used yet higher resolutions for comparisons.

3. Analytical expressions

The problem of steady flow in precessing ellipsoidal shells filled with a homogeneous fluid has been solved by analytical methods in the works of Stewartson & Roberts (1963), Roberts & Stewartson (1965) and Busse (1968). In the limit of the spherical shell the analytical solution is given by an Ekman layer flow at the solid boundary and by a rigid rotation with the angular velocity vector $\boldsymbol{\omega}$ in the interior of the shell. The analysis requires that the angle ε between the rotation vector $\hat{\boldsymbol{z}}$ of the shell and $\boldsymbol{\omega}$ is small since otherwise the Ekman boundary layer analysis is no longer valid. The critical latitudes which are located near 30° in the case of small precession rates $|\boldsymbol{\Omega}|$ cause a divergence of the Ekman boundary layer in any case (see, for example, Stewartson & Roberts 1963), but it is believed that this divergence has little influence on the expression for the vector $\boldsymbol{\omega}$ which is given by

$$\boldsymbol{\omega} = \hat{\boldsymbol{z}}\omega^2 + \omega^2[\hat{\boldsymbol{z}} \times \boldsymbol{\Omega}\, 2.62(E\omega)^{1/2} + \hat{\boldsymbol{z}} \times (\boldsymbol{\Omega} \times \hat{\boldsymbol{z}})(0.259(E/\omega)^{1/2} + \boldsymbol{\Omega} \cdot \hat{\boldsymbol{z}})]^{-1} \times [2.62^2 E\omega + (0.259(E/\omega)^{1/2} + \boldsymbol{\Omega} \cdot \hat{\boldsymbol{z}})^2] \quad (3.1)$$

for a full sphere. We have adopted the expression from Busse (1968) which differs slightly from that of Roberts & Stewartson (1965) because terms of the order ε^2 have been taken into account. When the term $0.259(E/\omega)^{1/2}$ is neglected the expression (3.1) describes the position of the vector $\boldsymbol{\omega}$ on a circular cone spanned by the vectors $\hat{\boldsymbol{z}}$ and $\boldsymbol{\Omega}$ such that the axis of the cone points in the direction of $\hat{\boldsymbol{z}} + \boldsymbol{\Omega}\,|\Omega|^{-1}$. As $|\boldsymbol{\Omega}|$ increases from zero the vector $\boldsymbol{\omega}$ is displaced from $\hat{\boldsymbol{z}}$ in the direction perpendicular to the meridional plane through $\hat{\boldsymbol{z}}$ and $\boldsymbol{\Omega}$ in the retrograde sense with respect to the rotation $\boldsymbol{\Omega} \times \boldsymbol{r}$. As $|\boldsymbol{\Omega} \cdot \hat{\boldsymbol{z}}|$ becomes large in comparison with $\sqrt{E}$, the rotation vector $\boldsymbol{\omega}$ of the fluid moves on the conical surface towards the direction of $\boldsymbol{\Omega}$. Owing to the term $0.259(E/\omega)^{1/2}$ the symmetry of the positions of $\boldsymbol{\omega}$ for positive and negative values of Ω is destroyed and the axis of the cone is slightly displaced.

4. Comparison between analytical and numerical results

In order to study the range of parameter values for which the expression is approximately valid a relatively large angle of 60° between $\boldsymbol{\Omega}$ and $\hat{\boldsymbol{z}}$ has been employed. The numerically determined vector $\boldsymbol{\omega}$ is obtained through an average of the poloidal component of the vorticity over the fluid sphere,

$$2\boldsymbol{\omega} = \langle \nabla \times (\nabla w \times \hat{\boldsymbol{r}}) \rangle + 2\hat{\boldsymbol{z}}, \quad (4.1)$$

where the angular brackets indicate the average over the fluid shell. The rotation vector can also be defined as a function of the radius r if the average is defined as the mean over surfaces $r = \text{const}$. We shall denote the fluid rotation vector $\boldsymbol{\omega}_F$ in this case. For numerical reasons the case of a fluid shell with $\eta = 0.01$ has been used as an approximation for the full sphere. The results are shown in figure 1 where the solid line indicates the intersection between the conical surface and the spherical surface. In order to indicate the slight asymmetry of the circular line its reflection with respect to the meridian connecting $\hat{\boldsymbol{z}}$ and $\boldsymbol{\Omega}$ has been indicated by the dashed line. As expected numerical and analytical results agree well for small values of $|\boldsymbol{\Omega}|$, but

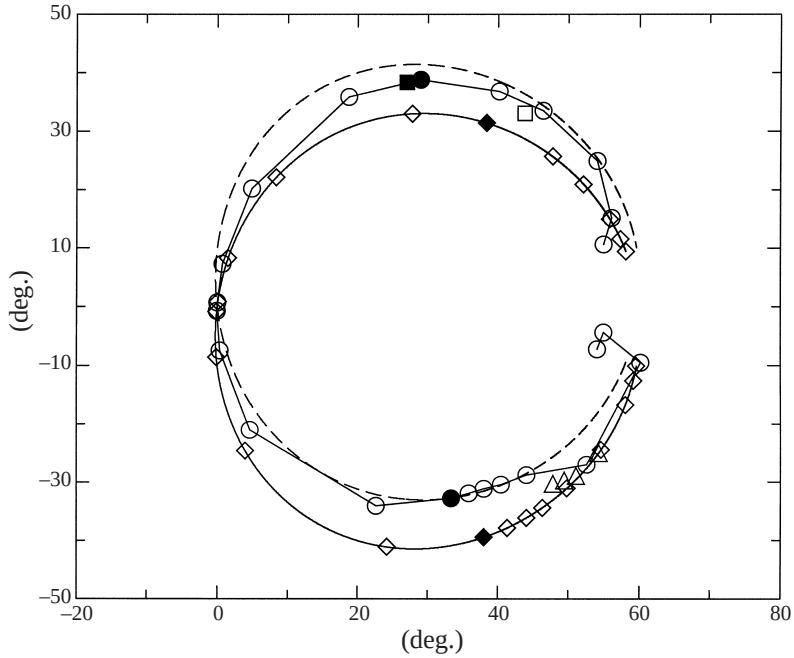

FIGURE 1. Direction of the average rotation vector $\boldsymbol{\omega}$ of the fluid given by the colatitude along the meridian connecting $\hat{\boldsymbol{z}}$ and $\boldsymbol{\Omega}$ (abscissa) and the colatitude along the perpendicular meridian (ordinate) as a function of the precession rate in the case $\alpha = 60°, \eta = 0.01$. Values based on the analytical expression (3.1) are indicated by diamonds, while numerical values obtained for $E = 5 \times 10^{-4}$ are given by circles for the same values of Ω. Starting at $(0, 0)$ $\Omega = \pm 10^{-3}, \pm 10^{-2}, \pm 0.03, \pm 0.07, \pm 0.1$ the last of which are indicated by filled symbols. The values $\Omega = -0.11, -0.12, -0.13$ have no corresponding values on the upper curves; the remaining diamonds and circles correspond to $\Omega = \pm 0.15, \pm 0.2, \pm 0.3, \pm 0.4$ and ± 0.5. Not connected by solid lines are the solutions obtained for $E = 3 \times 10^{-4}$ (filled square) and for $E = 10^{-4}$ (open square) for $\Omega = 0.07$. The four triangles correspond to $E = 8 \times 10^{-4}, 7 \times 10^{-4}, 6 \times 10^{-4}, 4 \times 10^{-4}$ (from left to right) for the case $\Omega = -0.2$.

significant differences appear as $|\boldsymbol{\Omega}|$ increases. Surprisingly the position of $\boldsymbol{\omega}$ follows the dashed line more closely than the solid line. Even at small angles between $\boldsymbol{\omega}$ and $\hat{\boldsymbol{z}}$ a difference between the analytical expression (3.1) and the numerical results can be expected since the effect of the divergence of the Ekman layer at the critical latitudes of $\pm 30°$ is only approximately taken into account in the analytical theories. Since the numerical results also exhibit considerable deviation from the rigid body rotation in the interior assumed as a basis for expression (3.1) the agreement shown in figure 1 must be regarded as rather good.

The variation of the direction of the fluid rotation vector $\boldsymbol{\omega}_F$ as a function of radius is shown in figure 2(*a*). Except for the expected rapid variation in the Ekman boundary layer the averaged vorticity approaches rigid body rotation throughout most of the interior. It is remarkable, however, that some variation of the direction occurs over the inner 3/5 of the radius while the direction is nearly constant for the outer 2/5 except for the Ekman boundary. Apparently the circulation driven by the Ekman suction is less efficient in the spin-over of the inner part of the fluid shell. The absolute value of $\boldsymbol{\omega}_F$ remains almost constant as a function of r if E is not too small as shown in figure 2(*b*). The interior values are somewhat higher than the values obtained from expression (3.1) which are 0.730, 0.673, 0.669, 0.579 in the same sequence as the curves from top to bottom. But when E decreases the spin-up process

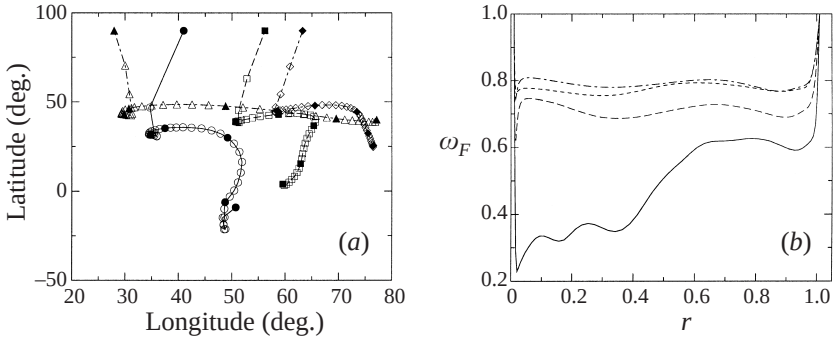

FIGURE 2. (*a*) The direction of the fluid rotation vector $\boldsymbol{\omega}_F$ as a function of r for $\Omega = 0.07, \alpha = 60^\circ$ for $E = 10^{-4}$ (circles), $E = 3 \times 10^{-4}$ (squares) and $E = 5 \times 10^{-4}$ (diamonds). Also shown is the case $\Omega = -0.07$ with $E = 5 \times 10^{-4}$ (triangles) for which the longitude scale has been shifted by $+90^\circ$. The longitude is zero and the latitude is 30° for the direction of the precession axis. The symbols correspond to equal distances in r over the interval $0.01 \leqslant r \leqslant 1.01$, and 41 steps in r are indicated with every eighth step denoted by a filled symbol. The point on the inner boundary adjacent to the lowermost filled symbol of each curve is not shown. (*b*) The absolute value ω_F of the fluid motion rotation vector as a function of r for $\alpha = 60^\circ, \eta = 0.01, \Omega = 0.07$. The solid, long-dashed and long-dash-short-dashed curves correspond to $E = 10^{-4}, 3 \times 10^{-4}$ and 5×10^{-4}, respectively. Also shown is the short-dashed curve for $\Omega = -0.07$ with $E = 5 \times 10^{-4}$.

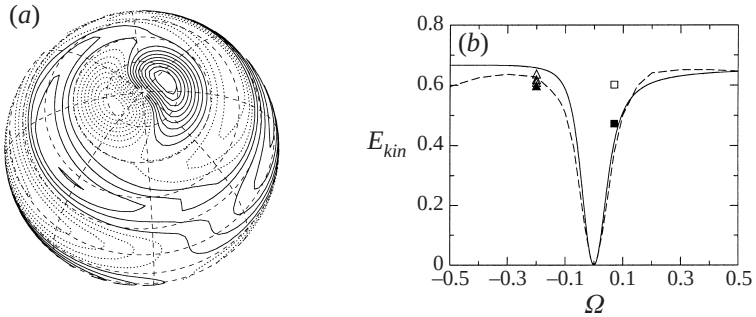

FIGURE 3. (*a*) Lines of constant radial component of the velocity field on the spherical surface $r = 0.75$ for $\Omega = -10^{-3}, \eta = 0.01, E = 10^{-4}, \alpha = 23.5^\circ$. The pole points in the direction of the $\hat{z}$-axis, while the axis of precession intersects the spherical surface directly below the pole. (*b*) The kinetic energy of the deviation of the fluid motion from the state of rigid rotation with the boundary as a function of Ω for $\alpha = 60^\circ$ with $E = 5 \times 10^{-4}$ (dashed line). The solid line indicates the theoretical result based on expression (3.1). The triangles indicate values obtained for $E = 4 \times 10^{-4}, 6 \times 10^{-4}, 7 \times 10^{-4}$ and 8×10^{-4} (from top to bottom). The open and filled squares indicate the kinetic energy obtained for $E = 10^{-4}$ and $E = 3 \times 10^{-4}$, respectively.

driven by the Ekman suction becomes inefficient and $\boldsymbol{\omega}_F$ decreases towards the centre as indicated by the solution obtained for $E = 10^{-4}$. An impression of the circulation induced by the Ekman suction can be gained from a plot of the radial component of the velocity field as shown in figure 3(*a*). The pattern which is reproduced after an inversion with respect to the centre of the sphere clearly exhibits its $m = 1$ structure.

Another comparison of analytical and numerical results is obtained through a presentation of the kinetic energy of the flow relative to the mantle frame. In figure 3(*b*) such a comparison is given which indicates that the largest discrepancy again occurs in the case of weak Ekman suction, $E = 10^{-4}$. When $|\Omega|$ is reduced, however, even a weaker Ekman suction is sufficient to induce an approximate rigid rotation in the interior in agreement with the presumption of the analytical theory of § 3.

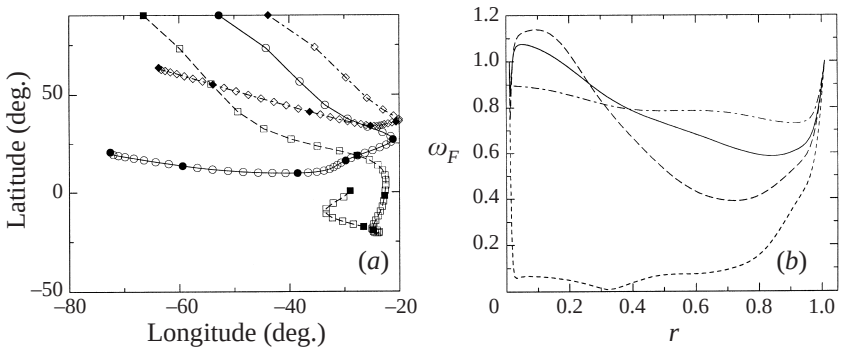

FIGURE 4. (*a*) The direction of the fluid rotation vector $\boldsymbol{\omega}_F$ as a function of r for $\Omega = -0.2, E = 7 \times 10^{-4}$ and $\alpha = 50°$ (diamonds), 60° (circles) and 70° (squares). The symbols correspond to equal distances in r over the interval $0.01 < r \leqslant 1.01$, and 41 steps in r are indicated with every eighth step denoted by a filled symbol. The point at $r = 0.01$ is not shown. (*b*) The absolute value ω_F of the fluid rotation vector as a function of r for the same cases as in (*a*). The short-dash-long-dash line, the solid line and the long-dash line correspond to the cases $\alpha = 50°$, 60° and 70°, respectively. Also shown by the short-dash line is the case $\Omega = -0.2, \alpha = 90°, E = 5 \times 10^{-4}$.

When the precession rate Ω becomes larger in absolute value, more significant deviations from a constant fluid rotation vector become noticeable. In figure 4(*a*) the results for three different angles α are shown in the case $\Omega = -0.2$. The direction of $\boldsymbol{\omega}_F$ moves to latitudes lower than that of $\boldsymbol{\Omega}$ for large portions of the interior and the absolute value ω_F also shows strong variations as indicated in figure 4(*b*). As the angle α approaches 90° the coherent rotation of the interior fluid nearly vanishes because the rotation imposed by the boundary is zero in the time average.

5. Precession-driven flows in spherical shells

When the inner radius of the spherical fluid shell is no longer negligibly small the analytical expression (3.1) can still be used when the conditions at the inner boundary are stress-free. A stress-free inner boundary is not realistic for planetary applications, but in principle it can be realized in an experiment through the use of a very light air-filled freely rotating concentric inner sphere. Since the fluid motion outside the inner sphere approaches solid body rotation and a nearly vanishing viscous torque is exerted on the inner sphere, the stress-free boundary is a valid approximation. Our main reason for adopting this boundary condition is that it simplifies the following analysis. Following the study of Busse (1968), we find that instead of extending the angular momentum type integrals over the entire sphere, the integrals need to be extended only over the fluid shell. This fact gives rise to a factor $(1 - \eta^5)$. After taking into account that the Ekman number is based on the thickness of the fluid shell we arrive at the conclusion that expression (3.1) is valid for a spherical fluid shell with radius ratio η and with stress-free inner boundary if $\sqrt{E}$ is replaced by $\sqrt{E}(1-\eta)/(1-\eta^5)$.

Computations carried out for $\eta = 0.9$ show fairly good agreement with the analytical expression (3.1) as is evident from table 1. The variation of the fluid rotation vector as a function of radius is much less than for the case of a full sphere. Except for the Ekman layer the angle of orientation of $\boldsymbol{\omega}_F$ varies by only 1° or less in latitude and by twice that amount in longitude. Similarly, the absolute value of the fluid rotation vector deviates by at most a few percent from its mean value througout the

External parameter		Position of averaged rotation vector		Absolute values ω of rotation vector
α (deg.)	Ω	colatitude θ (deg.)	longitude φ (deg.)	
23.5	−0.01	21.74 (20.80)	−40.13 (−35.70)	0.921 (0.935)
60	−0.01	49.39 (53.0)	−61.9 (−50.2)	0.625 (0.602)
60	−0.03	59.33 (60.33)	−25.24 (−17.7)	0.483 (0.495)
60	−0.003	21.80 (22.73)	−90.66 (−82.80)	0.921 (0.922)

TABLE 1. Comparison between numerical and analytical (given in brackets) results in the case of a precessing fluid shell with $\eta = 0.9, E = 10^{-4}$ and with inner stress-free boundary. $\varphi = 0$ corresponds to the position of the precession axis.

interior of the fluid shell. As expected the fluid rotation vector $\boldsymbol{\omega}_F$ differs less from the rotation vector $\hat{\boldsymbol{z}}$ of the two boundaries when boundary conditions are no-slip at both boundaries than when the inner boundary is stress-free.

An interesting feature exhibited by the numerical computations is the excitation of inertial oscillations in the 'polar' regions of the fluid shell, i.e. at latitudes higher than the critical ones on the inner boundary. These oscillations are stationary as seen from the precessing reference frame and do not seem to have a significant effect on the mean state of rotation of the fluid. A typical picture of the variation of the radial component of the velocity is shown in figure 5. In the precessing frame of reference the fluid flow can be described by

$$\tilde{\boldsymbol{u}} = \boldsymbol{\omega} \times \boldsymbol{r} + \boldsymbol{v} \equiv \boldsymbol{\omega} \times \boldsymbol{r} + \nabla \times (\nabla \times \boldsymbol{r}\chi) + \nabla \times \boldsymbol{r}\psi \tag{5.1}$$

where $\boldsymbol{\omega}$ is assumed to be a constant vector. The linearized equations for the small steady velocity field $\boldsymbol{v}$ are given by

$$\frac{\partial}{\partial \tilde{\varphi}}\boldsymbol{v} + 2(\boldsymbol{\Omega} + \boldsymbol{\omega}) \times \boldsymbol{v} = -\nabla\pi, \tag{5.2a}$$

$$\nabla \cdot \boldsymbol{v} = 0, \tag{5.2b}$$

where $\tilde{\varphi}$ denotes the azimuthal angle around the axis $\boldsymbol{\omega}$ and where we have neglected viscous friction. In the thin shell limit, $\eta \to 1$, the following equations for the scalar functions χ and ψ are obtained from the radial components of the curl and of the (curl)^2 of equation (2.1a) if $|\boldsymbol{\Omega}| \ll |\boldsymbol{\omega}|$ can be assumed:

$$\frac{\partial}{\partial \tilde{\varphi}}\nabla^2 L_2\chi + 2\boldsymbol{\omega} \cdot \nabla L_2\psi = 0, \quad \frac{\partial}{\partial \tilde{\varphi}}L_2\psi - 2\boldsymbol{\omega} \cdot \nabla L_2\chi = 0, \tag{5.3}$$

where L_2 is the negative Laplacian on the unit sphere, $L_2 \equiv r(\partial^2/\partial r^2)r - r^2\nabla^2$. In the polar regions where the approximation $\boldsymbol{\omega} \cdot \nabla \approx \omega\partial/\partial r$ holds, the solutions of equations (5.3) satisfying the boundary condition $\chi = 0$ at $r = r_i, r_o$ can be written in the form

$$\chi = P_{\tilde{l}}^1(\cos\tilde{\theta})\mathrm{e}^{\mathrm{i}\tilde{\varphi}} \cos\pi(r - \tfrac{1}{2}(r_i + r_o)), \tag{5.4a}$$

$$\psi = \mathrm{i}\pi\omega P_{\tilde{l}}^1(\cos\tilde{\theta})\mathrm{e}^{\mathrm{i}\tilde{\varphi}} \sin\pi(r - \tfrac{1}{2}(r_i + r_o)), \tag{5.4b}$$

where $\tilde{\theta}$ denotes the colatitude with respect to the axis $\boldsymbol{\omega}$. The latitudinal wavenumber $\tilde{l}$ is determined by

$$\tilde{l}(\tilde{l} + 1) = (4\omega^2 - 1)\pi^2(r_o + r_i)^2/4 \tag{5.4c}$$

and corresponds closely to the wavenumber exhibited by the patterns of figure 5(a, b).

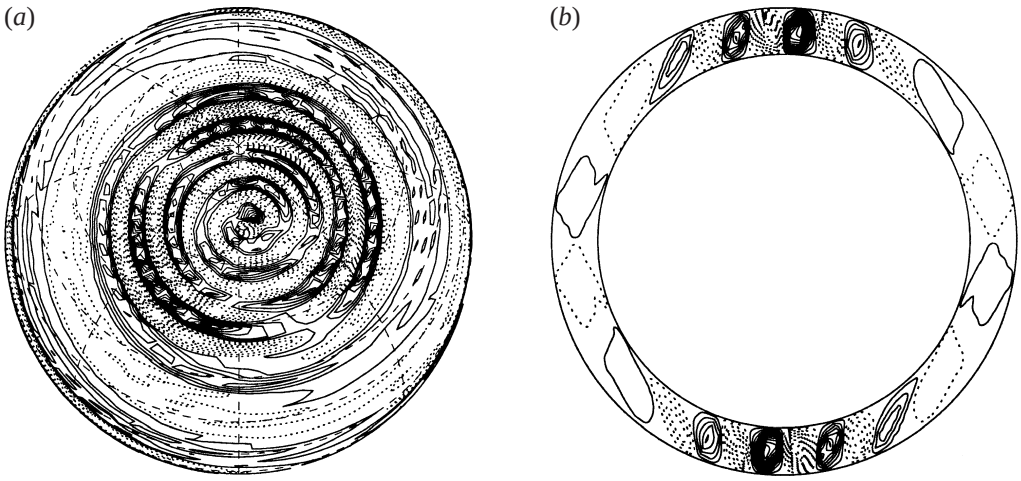

FIGURE 5. (*a*) Lines of constant radial velocity at the surface $r = 9.5$ in the case of a precessing fluid shell with $\eta = 0.9, \Omega = -0.003, \alpha = 60^\circ$ and $E = 10^{-4}$. The longitude of the precession axis is located in the middle of the plot. (*b*) Lines of constant radial velocity in the meridional plane spanned by the vectors $\hat{z}$ and $\boldsymbol{\Omega}$ for $\eta = 0.8, \Omega = -10^{-5}, \alpha = 23.5^\circ$ and $E = 10^{-4}$.

In the meridional cross-section shown in figure 5(*b*), the characteristic cone tangential to the critical latitude of the inner spherical boundary is clearly evident.

6. Instability of precession-driven laminar flows

While the steady state of solid body rotation of the fluid in the limit $\Omega \to 0$ is absolutely stable, hydrodynamic instabilities must be expected when deviations between the vectors of rotation of the boundary and of the fluid become sufficiently large. The choice of parameters used below is guided by the desire to obtain computationally well resolved simulations in which an instability of numerical origin can be excluded with certainty. Comparatively large Ekman numbers have therefore been used which imply large values of $|\boldsymbol{\Omega}|$ and α in order to drive the fluid sufficiently strongly. In experiments, the instability is localized at onset around internal cylindrical shear layers. Owing to the different set of control parameters, the instability in the simulations is fully three-dimensional and invades the entire fluid volume.

In the integrations in time of the precession-driven flow an instability has indeed been found which manifests itself in the form of an oscillation. In figure 6 the oscillation is exhibited in the plot of the kinetic energy of motion as a function of time for the case of a nearly full sphere ($\eta = 0.01$). The instability obviously corresponds to a supercritical Hopf bifurcation since the Reynolds number, which is proportional to E^{-1}, must exceed a critical value at which the sinusoidal oscillations set in with an infinitesimal amplitude. As E decreases the period of oscillation doubles as shown in figure 6(*a*) and finally a chaotic time dependence is realized as indicated in figure 6(*b*). The basic period of oscillation is still apparent in this latter figure.

The instability can be characterized by the symmetry it breaks. While the steady laminar basic state exhibits the symmetry property

$$\left.\begin{aligned} \psi(180^\circ - \theta, \varphi + 180^\circ) &= -\psi(\theta, \varphi), \\ \chi(180^\circ - \theta, \varphi + 180^\circ) &= \chi(\theta, \varphi), \end{aligned}\right\} \tag{6.1}$$

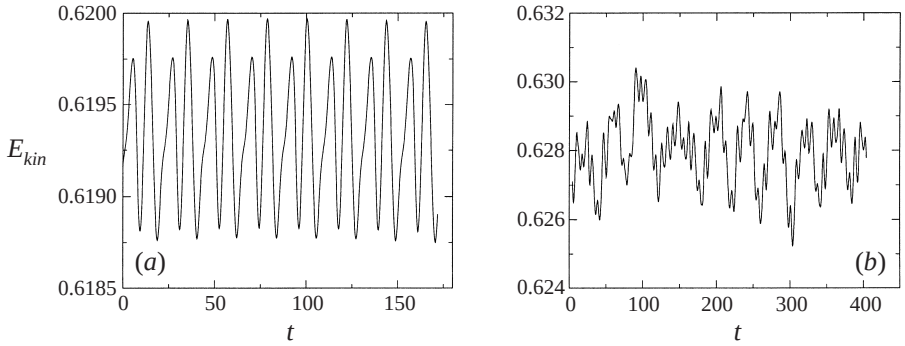

FIGURE 6. Time series of the kinetic energy E_{kin} in a full sphere ($r_i/r_o = 0.01$) with $\Omega = -0.2, \alpha = 60^\circ$. The Ekman number is 6×10^{-4} (*a*) and 5×10^{-4} (*b*).

η	E	α (deg.)	Ω	E_{kin}	E_a/E_{kin}	period
0.01	8×10^{-4}	60	−0.2	0.598	0	
0.01	7×10^{-4}	60	−0.2	0.6094	9.80×10^{-5}	10.4
0.01	6×10^{-4}	60	−0.2	0.619	1.16×10^{-3}	10.4 (PD)
0.01	5×10^{-4}	60	−0.2	0.628	2.33×10^{-3}	7.3 (CH)
0.01	4×10^{-4}	60	−0.2	0.638	3.3×10^{-3}	6.2 (CH)
0.01	7×10^{-4}	60	−0.15	0.559	0	
0.35	7×10^{-4}	60	−0.2	5.14	1.4×10^{-3}	4.4 (CH)
0.01	7×10^{-4}	50	−0.2	0.4697	0	
0.01	7×10^{-4}	70	−0.2	0.6897	4.6×10^{-3}	8.3 (CH)
0.01	5×10^{-4}	90	−0.2	0.7887	0	
0.01	3×10^{-4}	90	−0.2	0.846	1.3×10^{-2}	(CH)

TABLE 2. The total kinetic energy, E_{kin}, and the time average of the energy in the antisymmetric components, E_a, for shells with a ratio of inner to outer radii $\eta = r_i/r_o$ at the Ekman numbers E driven with the precession rate Ω about an axis which forms the angle α with the rotation axis of the shell. In the last column the basic oscillation period of the antisymmetric components is indicated which can also be determined when a period doubling (PD) or even a transition to a chaotic state (CH) has occurred. All runs used a resolution of 65 Chebychev polynomials and spherical harmonics up to $l = 64$ and $m = 32$.

when the representation $\boldsymbol{u} = \nabla \times \boldsymbol{r}\psi + \nabla \times (\nabla \times \boldsymbol{r}\chi)$ is used for the velocity field, the growing infinitesimal disturbances $\tilde{\boldsymbol{u}}$ exhibit the opposite symmetry,

$$\left.\begin{aligned} \tilde{\psi}(180^\circ - \theta, \varphi + 180^\circ) &= \tilde{\psi}(\theta, \varphi), \\ \tilde{\chi}(180^\circ - \theta, \varphi + 180^\circ) &= -\tilde{\chi}(\theta, \varphi). \end{aligned}\right\} \tag{6.2}$$

The time-averaged energy E_a of the components with the latter symmetry is a convenient indication of the instability. The ratio of E_a over the total kinetic energy E_{kin} is given in table 2. E_a/E_{kin} varies linearly with $E - E_c$, where E_c is the critical Ekman number. A surprising property of the instability is that it causes only minute deviations from the state of steady laminar flow even when E^{-1} approaches twice its critical value as evident from table 2. A large α and an inner core with $\eta = 0.35$ favour the instability. As can be seen from table 2 the energy E_a attains its largest value for $\alpha = 90^\circ$ when the fluid rotation $|\boldsymbol{\omega}|$ becomes rather small and the driving term is strongest.

7. Concluding remarks

The problem of the fluid flow in a precessing spherical cavity is one of the basic problems of fluid mechanics. Because of its potential planetary application, it as well as the more general problem of flow in a precessing spheroidal cavity had received much attention in the 19th century. It was long believed that a flow of constant vorticity as derived by Poincaré (see Lamb 1932) would be realized in the interior at least in the limit of vanishing viscosity. But the analysis of Busse (1968) demonstrated that the Poincaré solution does not correspond to the correct solution in the inviscid limit of the basic equation and that instead a tangential discontinuity of the interior velocity field must be expected. Since that time it has become clear that only through numerical analysis can a better understanding of the flows in precessing cavities be obtained. In this paper we have focused on the simplest of these problems, namely the flow in precessing spheres and spherical shells.

The main results of this paper are that the analytical formulas derived for the limit when the average vorticity of the fluid does not differ much from that of the boundary are approximately valid for a much wider regime than may have been expected. Moreover, they are applicable even in the case of a fluid shell after appropriate rescaling. A new phenomenon found in the case of thin spherical shells is standing inertial waves which appear to be excited by conditions near the critical latitude. Although instabilities of the basic flow have also been found they do not seem to lead to significant changes in the flow structure, at least not at the Ekman numbers that can be realized with the present numerical computations. It thus has not been possible to relate the instability found numerically to the experimentally observed ones. It must be kept in mind, though, that in all experiments mentioned in the literature such as, for instance, those of Malkus (1968) the ellipticity of the container exerts a larger influence than the Ekman boundary layer. With the growing capacity of computers even smaller Ekman numbers will become accessible and fully turbulent states of flow may be revealed by the computations.

REFERENCES

Busse, F. H. 1968 Steady fluid flow in a precessing spheroidal shell. *J. Fluid Mech.* **33**, 577–589.

Hollerbach, R. & Kerswell, R. R. 1995 Oscillatory internal shear layers in rotating and precessing flows. *J. Fluid Mech.* **298**, 327–339.

Lamb, H. 1932 *Hydrodynamics*, 6th edn. Cambridge University Press.

Malkus, W. V. R. 1968 Precession of the earth as the cause of geomagnetism. *Science* **160**, 259–264.

Roberts, P. H. & Stewartson, K. 1965 On the motion of a liquid in a spheroidal cavity of a precessing rigid body. II. *Proc. Camb. Phil. Soc.* **61**, 279–288.

Stewartson, K. & Roberts, P. H. 1963 On the motion of a liquid in a spheroidal cavity of a precessing rigid body. *J. Fluid Mech.* **17**, 1–20.

Tilgner, A. 1996 High-Rayleigh-number convection in spherical shells. *Phys. Rev.* E **53**, 4847–4851.

Tilgner, A. 1999*a* Spectral methods for the simulation of incompressible flows in spherical shells. *Intl J. Numer. Meth. Fluids* **30**, 713–724.

Tilgner, A. 1999*b* Magnetohydrodynamic flow in precessing spherical shells. *J. Fluid Mech.* **379**, 303–318.

Tilgner, A. & Busse, F. H. 1997 Finite amplitude convection in rotating spherical fluid shells. *J. Fluid Mech.* **332**, 359–376.